Journal of
Materials Chemistry B

ROYAL SOCIETY OF CHEMISTRY

PAPER

View Article Online
View Journal | View Issue

Check for updates

Cite this: *J. Mater. Chem. B*, 2026, **14**, 2324

Electroconductive and highly biocompatible PEDOT- and polypyrrole-alginate–gelatin hydrogels with enhanced electrochemical performance for biointerfaces

Karolina Cysewska,*[a] Lisa Schöbel[b] and Aldo R. Boccaccini[b]

Received 22nd September 2025,
Accepted 19th December 2025

DOI: 10.1039/d5tb02148k

rsc.li/materials-b

Conductive hydrogels are promising candidates for neural bioelectrodes due to their softness, ionic permeability, and reduced mechanical mismatch with neural tissue. However, pristine biopolymer matrices such as alginate–gelatin (Alg–GEL) lack sufficient electrical functionality. Here, Alg–GEL hydrogels incorporating PEDOT:PSS, polypyrrole (PPy/PSS), or both were developed *via* blending and *in situ* polymerization, yielding a tunable family of soft, electroactive materials. The hydrogels exhibited Young's moduli of 5–70 kPa, depending on polymer loading, while electrical conductivities ranged from 0.1 to 3.7 S cm^{-1}, with the highest values observed in PEDOT–PPy hybrids. Electrochemical measurements showed impedance values of 380–830 Ω cm^2 at 1 kHz, an electrochemical stability window of approximately −0.85 to +1.2 V *vs.* $Ag/AgCl_{sat}$, and current injection limits reaching 4 mA, comparable to platinum electrodes. Swelling studies indicated that PEDOT-modified hydrogels achieved 41–56% swelling after 24 hours. PPy-based hydrogels swelled to approximately 97% and hybrid systems showed behavior dependent on their composition. All conductive formulations demonstrated improved long-term stability compared to pristine Alg–GEL, which gradually lost mass over 28 days of incubation. In contrast, hydrogels containing PEDOT and PPy maintained nearly constant wet weight, consistent with the formation of interpenetrating networks that prevented polymer degradation and leaching. Biological evaluation with NIH3T3 fibroblasts showed that all hydrogels were cytocompatible. PPy-only and PPy–PEDOT hybrids supported higher metabolic activity and more attached and spread cells after 7 days compared to Alg–GEL, while PEDOT-only samples showed similar or slightly reduced cell activity. These results confirm excellent cytocompatibility and suggest that PPy-rich domains improve cell–material interactions. Overall, PEDOT- and PPy-modified Alg–GEL hydrogels offer high conductivity, softness, electrochemical stability, long-term durability, and biocompatibility, creating a versatile and adjustable platform for next-generation soft neural interfaces.

1. Introduction

Bioelectronics is a rapidly growing interdisciplinary field that sits at the intersection of materials science, electronics, and biology.[1,2] Its main goal is to create soft, compact, and flexible systems that can seamlessly integrate with living tissues, allowing for the sensing, stimulation, or modulation of biological signals.[3–5] As research advances toward next-generation medical devices and neural interfaces, there is an increasing need for materials that are not only biocompatible but also mechanically and electrically compatible with soft tissues.

A key application of bioelectronics is in neural recording and stimulation, which rely on implantable electrodes that directly interface with the brain.[5] Most clinically used electrodes are made from rigid metallic materials, such as platinum, iridium, or stainless steel. While these metals provide excellent electrical conductivity, they exhibit poor mechanical compatibility with neural tissue.[6] The significant mismatch in Young's modulus, often spanning several orders of magnitude, causes chronic inflammation, gliosis, and gradual signal loss. To overcome these issues, research has shifted toward developing soft, tissue-like materials that can reduce interfacial stresses and enhance long-term functionality.

Hydrogels have become promising contenders for bioelectrode matrices due to their high-water content, natural softness,

---

[a] *The Faculty of Electronics, Telecommunications and Informatics, and Advanced Materials Centre, Gdansk University of Technology, ul. Narutowicza 11/12, 80-233 Gdansk, Poland. E-mail: karolina.cysewska@pg.edu.pl*

[b] *Institute of Biomaterials, Friedrich-Alexander Universität Erlangen-Nürnberg, Cauerstraße 6, Erlangen 91058, Germany*

and adjustable mechanical properties.[7] These three-dimensional polymer networks can mimic the elasticity of brain tissue, offering flexibility, deformability, and low interfacial stress. Among natural polymers, alginate and gelatin are especially appealing due to their biocompatibility, biodegradability, and complementary properties.[8–10] Alginate, a linear anionic polysaccharide derived from brown algae, readily forms ionically cross-linked hydrogels in the presence of divalent cations, such as Ca^{2+}, resulting in mechanically stable networks under physiological conditions. Gelatin, a denatured form of collagen, provides bioactive motifs that support cell adhesion and enables thermoresponsive gelation. When combined, alginate and gelatin produce composite hydrogels with better structural strength and improved biological functions.

Despite these advantages, most hydrogels are naturally insulating, which limits their direct use in electronic or electrochemical devices, such as neural electrodes. To address this issue, recent efforts have focused on incorporating conductive components into hydrogel matrices.[11]

Conducting polymers, especially poly(3,4-ethylenedioxythiophene):polystyrene sulfonate (PEDOT:PSS) and polypyrrole (PPy), have shown significant promise due to their high conductivity, electrochemical stability, and biocompatibility.[12] PEDOT:PSS, and PPy conduct charge through fundamentally different but complementary mechanisms that enable efficient electronic transport when incorporated into hydrogel networks.[13] PEDOT and PPy are π-conjugated polymers, in which alternating single and double bonds allow charge carriers (polarons and bipolarons) to delocalize along the polymer backbone, providing electronic conductivity after oxidative doping. In PEDOT:PSS, the sulfonate groups of PSS act as polyanionic dopants that stabilize oxidized PEDOT chains, increase charge-carrier density, and improve dispersibility in water, enabling uniform mixing with hydrophilic hydrogel precursors.[14] In contrast, PPy dopes spontaneously during oxidative polymerization: chloride, PSS^-, or other anions enter the polymer during growth, balancing the positive charges on the PPy backbone and enabling efficient redox-based charge transport.[15] Together, these polymers contribute both electronic conductivity (*via* delocalized charge carriers) and enhanced ionic transport, making PEDOT- and PPy-modified hydrogels suitable for charge-transfer processes at bioelectronic interfaces. Therefore, hybrid hydrogel systems made from conducting polymers and hydrogels aim to merge the flexibility of hydrated polymer networks with the electronic conductivity required for active bioelectronic uses.

A variety of PEDOT-based hydrogels have been reported, but most face compromises between conductivity, mechanical compliance, and stability. For example, the *in situ* polymerization of PEDOT within a GelMA/chitosan matrix resulted in a hydrogel with a high elastic modulus (605 kPa) but limited conductivity (0.0018 S cm^{-1}).[16] An injectable PEDOT:PSS/acetic acid formulation achieved weak conductivity due to dilution of the commercial PEDOT:PSS stock (1.1 wt%) and showed poor retrievability from brain tissue.[17] PEDOT:PSS incorporated into polyacrylamide (PAAm) hydrogels provided moduli in the 10–100 kPa range; however, fabricating on rigid silicon substrates with gold/PDMS interconnects compromised the overall mechanical compliance.[18] Other strategies reported improved electrochemical performance: a PEDOT:PSS–poly(vinyl alcohol) hydrogel polymerized on platinum exhibited a modulus of 191 kPa and reduced impedance.[19] In contrast, a chemically polymerized PEDOT:PSS hydrogel containing Pln5-NH_2 achieved high conductivity (∼33 S cm^{-1}) with a very low modulus (∼200 Pa), although without data on stability or impedance.[20] Photocurable PEDOT:PSS hydrogels reached conductivities up to ∼20 S cm^{-1} with moduli around 10 kPa, but needed high PEDOT:PSS content (∼30 wt%).[21] Chemically synthesized PEDOT:PSS–alginate composites showed conductivity of ∼14 mS cm^{-1} but were excessively stiff (Young's modulus ∼0.4 GPa).[22] More recently, a PPEP hydrogel combining PVA, PAM, ethylene glycol, and *in situ* PEDOT achieved conductivity of ∼0.32 S cm^{-1} with good stretchability. However, its modulus was not optimized for neural interfacing.[23]

Taken together, these studies demonstrate that, although significant progress has been made in developing conductive hydrogels, achieving a good balance of conductivity, softness, stability, and biocompatibility remains challenging. There are few systematic comparisons of PEDOT-, PPy-, and hybrid formulations within the same hydrogel framework, and little is known about how their composition influences their combined mechanical, electrochemical, and biological performance.

To the best of our knowledge, no prior study has conducted a direct, systematic evaluation of Alg–GEL hydrogels modified with PEDOT, PPy, and their hybrids, including side-by-side comparisons of their mechanics, conductivity, electrochemical stability, long-term degradation, and cytocompatibility. Addressing this gap is crucial for advancing soft, conductive hydrogels toward dependable neural electrode applications.

In this study, a family of electroconductive hydrogels based on alginate–gelatin matrices, functionalized with PEDOT:PSS and/or PPy, was developed and thoroughly evaluated. Three fabrication methods were explored: (i) physical blending of PEDOT:PSS with the hydrogel precursor, (ii) *in situ* oxidative polymerization of pyrrole within the hydrogel network, and (iii) a combined hybrid approach combining both techniques. The resulting materials were systematically analyzed for their morphological, mechanical, electrical, electrochemical, and biological properties. The hydrogels showed electrical conductivities in the S cm^{-1} range, among the highest reported for hydrogel-based electrodes, along with broad electrochemical stability windows, high charge injection capacities, enhanced long-term stability, and verified cytocompatibility. These results position PEDOT- and PPy-modified alginate–gelatin hydrogels as promising candidates for next-generation soft neural interfaces, where safe charge transfer, durability, and tissue-like mechanics are essential.

2. Materials and methods

2.1. Chemicals and materials

The chemicals used in the work were sodium alginate (VIVAPHARM®, PH176, derived from Laminaria hyperborean, JRS PHARMA GmbH & Co. KG, Rosenberg, Germany), gelatine (from porcine skin, Gel strength 300, Bloom Type A), poly(sodium 4-styrene sulfonate) (NaPSS) (Mw ~ 70 000 g mol^{-1}) ($\geq$99%, Sigma Aldrich), PEDOT:PSS aqueous solution (1.3 wt%, Clevios PH1000), calcium chloride ($CaCl_2$) (powder, 99.99%), ammonium persulfate (APS) (ACS reagent, $\geq$98%). The pyrrole monomer (Sigma-Aldrich, reagent grade $\geq$98%) was purified immediately before use to remove oxidized impurities and stabilize the polymerization. Purification was accomplished by passing the neat monomer twice through a column of neutral aluminum oxide (Brockmann I, 50–200 μm, 60 Å, Acros Organics). Electrochemical measurements were performed in phosphate-buffered saline (PBS, pH 7.4), which consisted of 2.7 mM potassium chloride (KCl), 140.0 mM sodium chloride (NaCl), and 10.0 mM phosphate. PBS was purchased from Sigma-Aldrich. All solutions were prepared in Milli-Q water (>5 MΩ cm).

2.2. Synthesis of hydrogels

2.2.1. Alg–GEL hydrogels. Alginate–gelatin (Alg–GEL) hydrogels were prepared by separately dissolving sodium alginate (0.2 g in 5 mL) and gelatin (0.8 g in 10 mL) in ultrapure water under magnetic stirring. Alginate was stirred for 1 hour at room temperature, while gelatin was stirred for 10 minutes at 37 °C to ensure complete dissolution. Equal volumes of each solution (3 mL + 3 mL) were mixed under continuous stirring at 37 °C to create a uniform Alg–GEL blend. To form hydrogel disks, 200 μL of the Alg–GEL solution was pipetted into cylindrical molds, which had been pre-gelled by refrigeration for 10 minutes. Final cross-linking was achieved by immersing the samples in 0.1 M calcium chloride ($CaCl_2$) solution for 10 minutes to induce ionic gelation.

2.2.2. CP-based hydrogels. A schematic diagram of the hydrogel synthesis is shown in Scheme 1.

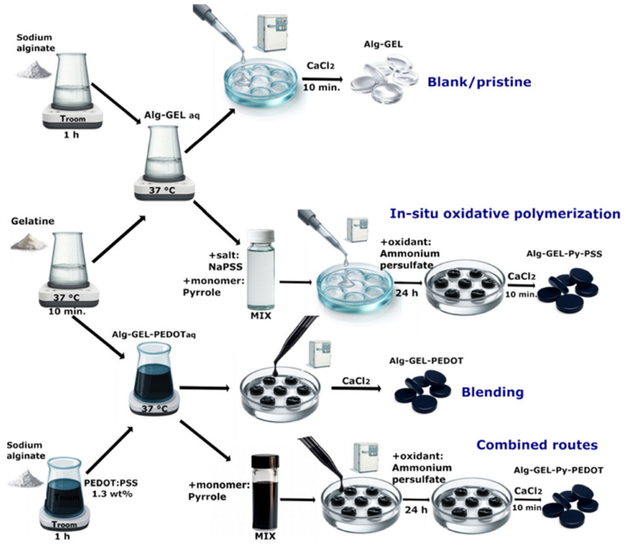

Scheme 1 Schematic diagram of the preparation routes for all hydrogel systems: pristine Alg–GEL (blank), Alg–GEL–PPy/PSS (*in situ* oxidative polymerization), Alg–GEL–PEDOT (blending), and Alg–GEL–PPy–PEDOT (combined). Representative photographs of the corresponding hydrogel samples are provided in the Supplementary Information (Fig. S1).

(a) Alg–GEL–PEDOT:PSS hydrogels: PEDOT:PSS-modified hydrogels were made by dissolving sodium alginate (0.2 g) in three different PEDOT:PSS/water mixtures: (a) 2 mL PEDOT:PSS solution (1.3 wt%) + 3 mL ultrapure water, (b) 3 mL PEDOT:PSS (1.3 wt%) solution + 2 mL water, and (c) 5 mL PEDOT:PSS (1.3 wt%) solution only. Each mixture was stirred magnetically for about 1 hour until a uniform Alg–PEDOT:PSS solution formed. Meanwhile, gelatin (1.2 g) was dissolved in 15 mL of ultrapure water at 37 °C for 10 minutes. The alginate–PEDOT:PSS dispersions were then combined with the gelatin solution in equal volumes (3 mL + 3 mL) and stirred at 37 °C to create the hydrogel precursor mixtures. Hydrogel discs were formed by casting 200 μL of each precursor into molds, followed by a pre-gelation step. Samples from mixture (a) were refrigerated for 10–15 minutes, while samples from mixtures (b) and (c), which had higher PEDOT:PSS content, were frozen for 10–15 minutes due to their lower gelation ability at colder temperatures. The discs were then cross-linked in 0.1 M $CaCl_2$ for 10 minutes to stabilize the network.

(b) Alg–GEL–PPy–PSS hydrogels: to prepare *in situ* polymerized polypyrrole (PPy) hydrogels, 0.8 g of sodium alginate was dissolved in 20 mL of ultrapure water under stirring for 1 hour, and 1.2 g of gelatin was separately dissolved in 15 mL of ultrapure water at 37 °C for 10 minutes. After mixing 3 mL of alginate solution with 3 mL of gelatin solution, four formulations (a–d) were obtained by varying the concentrations of the dopant and monomer. Sodium polystyrene sulfonate (NaPSS) was added at two concentrations: 2.5 mg mL^{-1} (15 mg per 6 mL) for formulations a and b, and 4.0 mg mL^{-1} (24 mg per 6 mL) for formulations c and d. Each mixture was stirred for 5–10 minutes until a uniform blend was achieved. Pyrrole monomer was then added at either 0.1 M (41.2 μL per 6 mL) or 0.2 M (82.4 μL per 6 mL), depending on the formulation, and the samples were vigorously shaken and briefly stirred to initiate monomer distribution within the hydrogel matrix. Hydrogel disks were formed by pipetting 200 μL of each mixture into molds and refrigerating for 10–15 minutes to initiate physical gelation. Polymerization was initiated by adding ammonium persulfate (APS) as the oxidizing agent: either 1.149 g or 2.28 g of APS was dissolved in 20 mL of ultrapure water, depending on the pyrrole concentration. The polymerization process continued overnight at room temperature. The resulting samples were washed sequentially with 70% ethanol for 1-hour, ultrapure water (three times for 5 minutes each), and Hank's Balanced Salt Solution (HBSS, Gibco, Thermo Fisher, Germany) following this schedule: twice for 30 minutes, four to five times for 1 hour, overnight soaking in HBSS, and a final exchange with fresh HBSS for an additional hour. After purification, the hydrogels were cross-linked by immersion in 0.1 M $CaCl_2$.

(c) Hybrid Alg–GEL–PPy–PEDOT:PSS hydrogels: hybrid hydrogels combining both PEDOT:PSS and *in situ* polymerized PPy were prepared using a multistep approach. First, sodium alginate (0.4 g) was dissolved in three different PEDOT:PSS/water mixtures: (a) 4 mL PEDOT:PSS + 6 mL water, (b) 6 mL PEDOT:PSS + 4 mL water, and (c) 10 mL PEDOT:PSS only. Each solution was stirred for 1 hour to obtain homogeneous

Alg–PEDOT:PSS dispersions. In parallel, gelatin (1.2 g) was dissolved in 15 mL of ultrapure water at 37 °C for 10 minutes. The alginate–PEDOT:PSS and gelatin solutions were then combined in equal volumes (3 mL + 3 mL), resulting in six hydrogel formulations (a–c and a′–c′), which varied in pyrrole concentration. Pyrrole was added to each formulation at either 0.1 M (41.2 μL/6 mL) or 0.2 M (82.4 μL/6 mL), followed by vigorous shaking and mixing on a magnetic stirrer for 5 minutes. The pre-gelation step was performed by refrigeration for 10–15 minutes for samples a/a′, or by freezing for samples b–c′, depending on their PEDOT:PSS content. Pyrrole polymerization was initiated by adding APS (1.149 g or 2.28 g per 20 mL of ultrapure water) and allowing the reaction to proceed overnight. The resulting hydrogels underwent the same cleaning procedure as described for the PPy–PSS samples: ethanol (70%, 1 hour), ultrapure water (3 × 5 minutes), and HBSS in multiple cycles with overnight soaking, followed by a final HBSS exchange. The final step involved cross-linking with 0.1 M $CaCl_2$ to stabilize the structure.

2.3. Physico-chemical and mechanical characterizations

For morphology and structure tests, hydrogel samples were frozen in liquid nitrogen and then lyophilized using a freeze dryer (Alpha 1–2, LDplus) at −70 °C and 0.8 mbar for at least 24 hours. Subsequently, the samples were coated with a thin 10 nm gold layer.

The surface morphology of the samples was examined using scanning electron microscopy (SEM) (FEI QUANTA FEG 250) equipped with an energy-dispersive X-ray spectroscopy (EDS) detector. Imaging was performed in backscattered electron (BSE) mode at 10 kV with various magnifications. EDS was used to analyze the chemical composition of the samples. The accelerating voltage was increased from 10 to 15 kV for EDS mapping. Fourier-transform infrared spectroscopy (FT-IR) was conducted using a Bruker INVENIO spectrometer with an attenuated total reflectance (ATR) module featuring a germanium crystal. FT-IR spectra were recorded over a wavenumber range of 600–4000 cm^{-1}, with 128 scans averaged for each measurement.

2.4. Mechanical characterization

The mechanical properties of the hydrogel were measured using unconfined compression testing with a universal testing machine (Instron 5967, Instron GmbH, Germany). Hydrogel samples were tested as the as-prepared cylindrical discs with a diameter of 9 mm and a thickness of 2 mm (measured individually before each test; mean thickness 2 mm ± 0.2 mm). The samples were compressed at a rate of 1 mm min^{-1} up to a maximum strain of 20%. The effective compressive modulus was calculated from the slope of a linear fit applied to the data within a strain range of 5% to 10%. Compression was intentionally limited to 20% strain to remain within the small-strain, quasi-linear regime, where hydrogels exhibit stable elastic behavior and modulus values are most relevant for assessing mechanical compatibility with soft tissues.[24,25] At higher strains, hydrogels undergo nonlinear structural changes, such as densification, pore collapse, and fluid expulsion, rendering modulus measurement unreliable for biointerface design.

To examine the stress-relaxation behavior of the hydrogel films, the force was held constant and recorded for 120 seconds after compressing to 20% strain. The effective compressive modulus and stress relaxation behavior were determined using $n = 4$ samples.

2.5. Electrical and electrochemical studies

The electrical conductivity of the samples was measured using the 4-point van der Pauw resistivity method at room temperature in a synthetic air atmosphere. The hydrogel discs were placed into a custom-made cell with four silver pins (silver paste, DuPont 4922 N, USA) (Fig. S2). This prepared cell with the sample was then placed in a sealed chamber to maintain environmental stability (at room temperature in a synthetic atmosphere) (Fig. S3) and connected to a Keithley 2400 source meter. Electrochemical measurements were performed in a three-electrode, water-jacketed glass cell linked to a potentiostat (VersaSTAT 4). Hydrogel discs (9 mm diameter, 2 mm +/− 0.2 mm thickness) served as the working electrodes. Each disc was clamped at its mid-plane inside a Pt–Teflon holder so that only the lower half of the hydrogel cylinder was exposed to the electrolyte, while the upper half remained fixed inside the holder (Fig. S4). In this setup, the entire submerged half of the hydrogel acted as the electrochemically active surface, and no metallic parts of the holder contacted the solution. Before each electrochemical measurement, the thickness of each hydrogel disc was measured, and the geometric active area was calculated for each disc and used for normalization. A saturated Ag/AgCl electrode (KClsat, BioLogic) and a Pt mesh acted as the reference and counter electrodes, respectively. The electrolyte was phosphate-buffered saline (PBS), and the temperature was maintained at 37 ± 0.1 °C using a thermostat (Julabo F12). The interfacial impedance $|Z|$ of the samples was determined using electrochemical impedance spectroscopy (EIS) over the frequency range of 10 kHz–0.1 Hz, with a sinusoidal perturbation of 5 mV rms. The potential stability window and redox activity of the hydrogels were determined by cyclic voltammetry (CV) between −1.2 and +1.2 V *vs.* Ag/AgCl, with five consecutive cycles recorded at a scan rate of 50 mV s^{-1}. Stimulation performance was evaluated from potential transient measurements under biphasic current pulsing. The applied waveform consisted of a cathodic pulse (−I, 1 ms), followed by a short interpulse interval (0 A, 20 μs), and then an anodic pulse (+I, 1 ms). The electrode polarization was monitored *vs.* $Ag/AgCl_{sat}$, and the current injection limit (CIL) was defined as the highest current at which the electrode potential remained within the water stability window determined by CV.

All electrochemical tests were repeated at least three times, and the results are reported as averages with their corresponding standard deviations and relative errors. The statistics were evaluated using OriginPro. All electrochemical data are normalized to a geometric electrode area of 1 cm^2, ensuring full comparability between samples.

2.6. Biological studies

2.6.1. Cell maintenance.

NIH3T3 fibroblast cells were used to evaluate the cytocompatibility of the developed hydrogels, as fibroblast cell lines are commonly employed in ISO-10993–compliant cytotoxicity testing and serve as standard models for initial biocompatibility screening of biomaterials.[26] The cells were grown in T75 flasks in an incubator set at 37 °C, 5% CO_2, and 95% humidity. The cell culture medium (CCM) consisted of high-glucose Dulbecco's Modified Eagle Medium (DMEM, 4.5 g L^{-1} glucose, [+] L-Glutamine, [+] Na-Pyruvate, Gibco, Thermo Fisher), supplemented with 10 v/v% bovine calf serum (BCS) and 1 v/v% penicillin/streptomycin (PS). The cells were passaged every 2 to 3 days. For cell counting, cells were detached with trypsin and counted in a Neubauer chamber.

2.6.2. Cell seeding. After preparing the hydrogel films, the samples were washed repeatedly with HBSS until the supernatant pH was neutral and stable. Then, the hydrogels were sterilized by soaking in 70% ethanol for 1 hour, followed by three washes with HBSS for 5 minutes each. Next, the samples were immersed in CCM and incubated at 37 °C, 5% CO_2, and 95% humidity for 2 hours. After incubation, the medium was removed, and 50 000 cells per sample were seeded onto the hydrogel films in 100 μL. The samples were then incubated at 37 °C for 30 minutes to promote initial cell attachment. Finally, 1 mL of CCM was added to cover the cell-seeded samples, which were then incubated for up to 7 days in an incubator, with medium changes performed three times a day.

2.6.3. Cell activity by colorimetric assay. After 1 and 7 days of incubation, a colorimetric WST-8 assay was performed to assess NIH3T3 cell proliferation. For this, the cell culture medium was removed, and the cell-seeded samples were transferred to new well plates to eliminate the effect of cells grown on the tissue culture polystyrene surface. Subsequently, a 3% (v/v) WST-8 solution in CCM was added, and the samples were incubated at 37 °C, 5% CO_2, and 95% humidity. After 3 hours of incubation, 100 μL of supernatant was collected from each sample in triplicate and transferred to a 96-well plate. Finally, the absorbance at 450 nm was measured using a plate reader (FLUOstar Omega, BMG Labtech).

2.6.4. Calcein-DAPI staining and fluorescent microscopy. After performing the WST-8 assay, the residual WST-8 solution was removed, and the cells were stained with a 4 μL mL^{-1} Calcein-AM solution in HBSS by immersion and incubation for 45 minutes at 37 °C, 5% CO_2, and 95% humidity. Subsequently, the Calcein-AM solution was removed, and the cells were fixed for 15 minutes at room temperature with 4% (v/v) paraformaldehyde in HBSS. Next, the samples were immersed in 1 μL mL^{-1} DAPI solution in HBSS at room temperature for 30 minutes. Finally, the DAPI solution was replaced with HBSS, and the hydrogels were stored at 4 °C until fluorescence microscopy (AXIO Observer.D1, Carl Zeiss Microscopy, Germany) was performed.

2.7. Swelling and mass-retention behavior

Since drying Alg–GEL hydrogels causes irreversible structural collapse, dry-weight degradation analysis was not conducted. Instead, long-term stability was evaluated through swelling behavior and wet-mass retention, which are commonly used for ionically cross-linked and conductive hydrogels under physiologically relevant hydrated conditions.[27,28]

After preparing the hydrogel films, the samples were washed repeatedly with HBSS until the collected supernatants reached a neutral and stable pH. The ready-to-use samples were sterilized by immersing them in 70% ethanol for 1 hour, followed by three washing cycles with sterile HBSS under a sterile laminar flow hood. Next, the samples were transferred into pre-weighed cell strainers and weighed to determine the initial weight (w_0). Subsequently, the samples were immersed in Dulbecco's Modified Eagle Medium (DMEM, 4.5 g L^{-1} glucose, [+] L-Glutamine, [+] Na-Pyruvate, Gibco, Thermo Fisher) supplemented with 1 v/v% penicillin/streptomycin (PS) and placed in an incubator set at 37 °C, 5% CO_2, and 95% humidity. At the specified time points, the samples were removed from the medium, gently dried with autoclaved tissue paper, and weighed again (w_t). The weight change can be calculated using the following formula:

$$\text{Weight change }(\%) = \frac{w_t - w_0}{w_0} \times 100$$

The medium was exchanged three times a week to remove degradation products and to mimic cell culture conditions. The weight change was determined using n = 3 samples.

3. Results and discussion

3.1. Fabrication and structural characterizations of the hydrogels

SEM imaging revealed distinct structural differences between pristine Alg–GEL hydrogels and those modified with conducting polymers (Fig. 1 and 2). The Alg–GEL control displayed a relatively smooth, porous structure with thin, interconnected wls and large open spaces, typical of polysaccharide–protein hydrogels.[29] Adding PEDOT:PSS altered this structure in a concentration-dependent manner. At low PEDOT levels (PEDOT4) (Fig. 1B), fibrous, web-like deposits appeared across the pore surfaces, making the network appear denser. At medium loading (PEDOT6) (Fig. 1C), the structure became more compact and granular, adopting a cauliflower-like morphology, which is typical for PEDOT,[30] with fewer visible

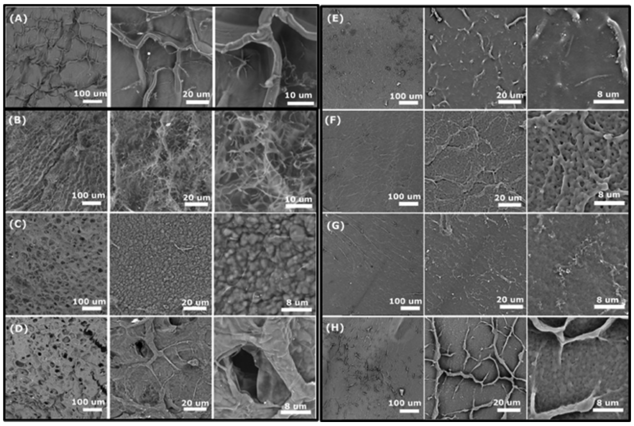

Fig. 1 SEM images of Alg–GEL (A), Alg–GEL: –PEDOT4 (B), –PEDOT6 (C), –PEDOT10 (D), –Py0.1PSS2.5 (E), –Py0.1PSS4 (F), –Py0.2PSS2.5 (G), and –Py0.2PSS4 (H) with different magnifications.

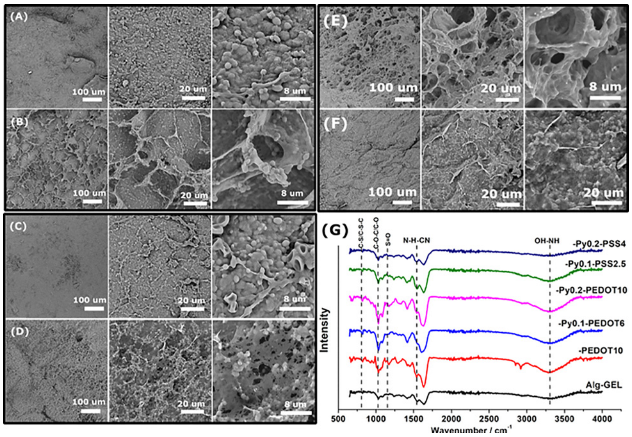

Fig. 2 SEM images of Alg–GEL: –Py0.1PEDOT4 (A), –Py0.2PEDOT4 (B), –Py0.1PEDOT6 (C), –Py0.2PEDOT6 (D), –Py0.1PEDOT10 (E), –Py0.2PEDOT10 (F) with different magnifications, and FTIR analysis of selected hydrogels (G).

pores, indicating PEDOT-rich clusters partially filled the network. At the highest level (PEDOT10), the hydrogel exhibited a solid, rigid network with thick walls and some collapsed cavities, suggesting ongoing densification of the matrix (Fig. 1D).

A different trend was observed in the PPy/PSS hydrogels. At low pyrrole content with 2.5 mg mL^{-1} NaPSS, the structure remained relatively smooth, featuring fine vein-like networks but without significant pore collapse (Fig. 1E). Increasing PSS concentration to 4 mg mL^{-1} promoted the formation of interconnected channels and more granular domains, giving a rougher appearance (Fig. 1F). When the pyrrole feed was raised to 0.2 M at low PSS, the morphology became less uniform, with fibrillar aggregates and heterogeneous PPy clusters dispersed across the surface (Fig. 1G). Combining high pyrrole and high PSS produced the most developed PPy structures, with compact ridges and PPy-rich regions throughout the matrix, consistent with extensive *in situ* polymerization (Fig. 1H).

The hybrid PEDOT–PPy systems combined features of both behaviors. At low pyrrole concentration with PEDOT4, the morphology stayed quite smooth with only sparse granular areas, indicating limited PPy deposition (Fig. 2A).

Increasing pyrrole to 0.2 M resulted in larger, irregular cavities and fibrillar clusters, making the structure rougher and more varied (Fig. 2B). In PEDOT6-based samples, low pyrrole loading created solid surfaces decorated with spherical nodules (Fig. 2C). In contrast, higher pyrrole levels caused more irregular and porous structures, with extensive granular coverage and partially collapsed pores (Fig. 2D). For PEDOT10 hybrids, combining low pyrrole content produced sponge-like, porous networks with thick ridges (Fig. 2E). Conversely, higher pyrrole levels created the most varied surfaces, mixing compact granular coatings with vein-like fibrillar networks that partially blocked the hydrogel pores (Fig. 2F).

Overall, the addition of PEDOT to the Alg–GEL matrix resulted in a denser network, thickening the pore walls and partially collapsing the porous structure, particularly at higher PEDOT loadings. In contrast, PPy/PSS polymerization produced granular and fibrillar domains, with higher pyrrole and PSS levels resulting in rougher, more uneven morphologies. The hybrid formulations demonstrated an interaction between these processes: PEDOT helped to compact and strengthen the hydrogel matrix, while PPy contributed distinct, granular, redox-active regions. The morphology of the hybrids depended on the PEDOT-to-PPy ratio, with PEDOT-dominant systems appearing more compact and smoother, and PPy-rich systems showing greater heterogeneity and fibrillar features. Supporting EDX analysis confirmed these patterns, showing a uniform element distribution across the hydrogel surface and sulfur signals in PEDOT- or PPy-containing samples, which were absent in the original Alg–GEL control (Fig. S5, SI).

FTIR spectroscopy was carried out to confirm the presence of the individual polymeric domains and to identify the characteristic bonding interactions within the hydrogel structure (Fig. 2G). The reference Alg–GEL spectrum shows the expected hydrogel bands: a broad O–H/N–H stretching envelope at approximately 3300–3500 cm^{-1} (alginate, gelatin, bound water), amide I at around 1645–1660 cm^{-1} (C=O, overlapping with the H–O–H bending of water), amide II near 1540 cm^{-1} (N–H bending/C–N stretching), and the carboxylate bands of alginate at roughly 1590–1610 cm^{-1} (ν_asCOO^{-}) and 1405–1425 cm^{-1} (ν_sCOO^{-}).[31,32] The polysaccharide backbone produces strong C–O–C/C–O vibrations in the 1060–1030 cm^{-1} range.[33]

Upon incorporating PEDOT:PSS (Alg–GEL–PEDOT10), new or intensified features appear at approximately 1190–1200 and 1120–1140 cm^{-1}, attributed to the ethylenedioxy C–O–C stretching of PEDOT and S=O stretching of sulfonate groups in PSS.[34] Additionally, a strengthened band around 1060–1030 cm^{-1} overlaps with alginate C–O and PSS S=O. Further signatures emerge at roughly 700–900 cm^{-1}, representing C–S/C–S–C of the thiophene ring and aromatic C–H out-of-plane bending from PSS. Minor shifts and shape changes in ν_as/s(COO^{-}) and amide I/II bands, along with broadening of the O–H/N–H envelope, indicate non-covalent interactions—namely, electrostatic complexation of PSS^{-} with –NH$_3^+$ sites on gelatin and altered hydrogen bonding with alginate and gelatin,[35,36] thus confirming the physical anchoring of PEDOT:PSS within the matrix.

For the PPy-containing hydrogels (Alg–GEL–Py0.1–PSS2.5 and Alg–GEL–Py0.2–PSS4), the ATR-FTIR spectra exhibit the characteristic Alg–GEL bands, including ~1635 cm^{-1} (ν_as(COO^{-}) of alginate overlapped with amide I ν(C=O) and ν(N–H) coupling from gelatin), 1427 cm^{-1} (ν_s(COO^{-}) of alginate), and ~1026 cm^{-1} (C–O–C stretching of the alginate-derived 1,4-β-glycosidic linkages).[37,38] The broad band at ~3462 cm^{-1} is attributed to O–H and N–H stretching vibrations of alginate, gelatin, and polypyrrole, while the peak at ~2858 cm^{-1} corresponds to aliphatic C–H stretching of the biopolymer backbones and PPy.[37] In addition, two low-intensity PPy-specific bands are observed at ~1295 cm^{-1} and ~933 cm^{-1}, assigned to in-plane and out-of-plane C–H deformation modes of the polypyrrole ring, respectively. The relative intensity of the PPy marker bands increases with higher pyrrole and NaPSS content, indicating greater PPy loading in the hydrogel matrix.

Hybrid samples combining PEDOT:PSS with *in situ* PPy (Alg–GEL-Py0.1PEDOT6 and Alg–GEL-Py0.2PEDOT10) display an essentially additive spectral signature of both conducting phases: (i) PEDOT/PSS markers at approximately 1190–1120 and 1060–1030 cm^{-1} along with 700–900 cm^{-1} (thiophene C–S); and (ii) PPy markers in the range of roughly 1540–1500, 1300, and 1180–1040 cm^{-1}. The relative intensities increase with the monomer/polymer content (from Py 0.1 M/PEDOT6 to Py 0.2 M/PEDOT10). At the same time, the envelopes of alginate carboxylate and gelatin amide display subtle shifts and shape changes, consistent with cumulative electrostatic (PSS$^-$ ↔ –NH$_3^+$/screened COO$^-$) and hydrogen-bonding interactions. No new resonances indicating covalent grafting are observed across the series.

Taken together, the FTIR data (i) confirm the successful incorporation of PEDOT:PSS and/or NaPSS-doped PPy into the Alg–GEL network, (ii) provide evidence of non-covalent anchoring of the conducting phases through electrostatic complexation and hydrogen bonding rather than covalent bonds, and (iii) demonstrate composition-dependent spectral growth of PEDOT and PPy fingerprints, supporting the formation of percolated conductive domains in hybrid formulations.

The compressive Young's modulus (E) varied significantly with both the type and the amount of the conducting polymer phase (Fig. 3a). The pristine Alg–GEL network exhibited an intermediate stiffness ($E \approx 8$ kPa), observed in an ionically crosslinked, highly hydrated biopolymer hydrogel.[39] Adding low to moderate amounts of PEDOT:PSS (PEDOT4, PEDOT6) did not significantly change E, while high PEDOT:PSS loading (PEDOT10) caused a notable decrease in stiffness. This suggests that excess PSS$^-$ counterions disrupt ionic crosslinking between alginate COO$^-$ groups and Ca^{2+}, increase water absorption, and plasticize the network.

In contrast, *in situ* polymerization of polypyrrole (PPy) within the Alg–GEL matrix significantly increased E (up to about 3–4 times the Alg–GEL value), consistent with PPy acting as a rigid, particulate reinforcement and adding additional physical cross-linking points. This stiffening effect was observed for both low and high pyrrole/PSS loadings, although samples with higher PSS content showed slightly lower E, likely due to increased hydration.

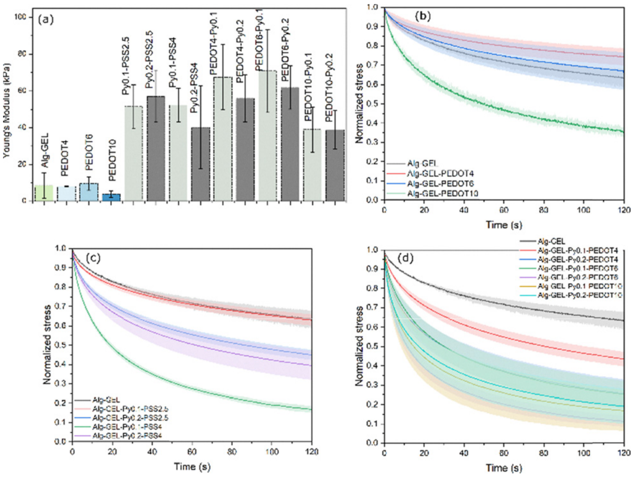

Fig. 3 Young modulus (a) and stress relaxation results (b)–(d) of hydrogels.

Hybrid systems combining PEDOT:PSS and PPy showed the highest stiffness values in the dataset. Specifically, formulations with moderate PEDOT:PSS loading (PEDOT4–6) and low PPy concentration (0.1 M) achieved the highest modulus, indicating a synergistic effect between the two conducting phases: PEDOT:PSS helps with dispersion and integration of PPy domains, while PPy adds rigid reinforcement. However, when PEDOT:PSS loading was increased to PEDOT10, the modulus decreased compared to these optimal hybrids, highlighting the adverse plasticization effect of excess PSS.

Stress relaxation tests under constant compressive strain (Fig. 3b–d) showed apparent differences in viscoelastic behavior. The normalized stress σ/σ_0 after 120 seconds (S_{120}) was used as a comparison parameter. Pristine Alg–GEL maintained approximately 65% of its initial stress at 120 seconds, indicating a balance between elastic recovery and viscous dissipation in its ionically cross-linked network.

For PEDOT-only samples, relaxation accelerated with higher PEDOT:PSS content: PEDOT4 and PEDOT6 had S_{120} values similar to Alg–GEL. At the same time, PEDOT10 relaxed the fastest ($\sim$35%), matching its lower modulus and more viscous network structure caused by excess PSS.

PPy-only hydrogels exhibited a higher modulus but relaxed faster than Alg–GEL, maintaining approximately 45–15% of stress after 120 seconds. This indicates that while PPy quickly stiffens the network, the presence of PPy domains and related counterions increases internal interfaces, promoting local sliding or rearrangement and thereby enhancing time-dependent stress dissipation.

Hybrid PEDOT + PPy formulations combined the highest stiffness with relatively fast relaxation. The S_{120} values were among the lowest in the dataset, especially at high PPy loadings, indicating that these double-network-like structures store a large amount of initial elastic stress but also provide multiple dissipation pathways, including polymer chain rearrangement, reversible hydrogen bond rupture, and interfacial sliding between PEDOT, PPy, and Alg–GEL phases.

These results suggest that high instantaneous stiffness does not always lead to slower stress relaxation. In this system, the microstructural source of stiffness (rigid filler *versus* ionic crosslinking) and the hydration and counterion environment influence the viscoelastic response. Achieving an optimal balance of both properties for bioelectrode applications will require adjusting the conducting polymer content to provide sufficient mechanical support without excessive viscous dissipation during long-term cyclic loading.

Although repeated mechanical cycling tests were not conducted in this study, the long-term mechanical behavior of alginate-based hydrogels under cyclic compression is well documented in the literature. Prior studies have shown that alginate and alginate–gelatin hydrogels may experience a slight decrease in apparent modulus during the initial loading cycle, which is usually due to partial dissociation of Ca^{2+}–alginate ionic crosslinks, disruption of physical interactions in gelatin, and local water redistribution within the network. Importantly, this effect is typically limited to the first cycle, after which the mechanical response stabilizes.

Abroug *et al.*[40] reported stabilization of the compressive response of alginate hydrogels after the first loading cycle using the same alginate grade as in the present study, indicating that further cyclic deformation does not lead to ongoing mechanical degradation. Likewise, Zhang *et al.*[41] demonstrated similar cyclic behavior in alginate-based hydrogels reinforced with polypyrrole nanospheres, suggesting that adding a conductive polymer phase does not fundamentally change the fatigue response of the alginate network.

Given that neural interfaces generally operate within small strain amplitudes, the mechanical stability observed for alginate-based hydrogels under cyclic loading supports the suitability of the developed conductive hydrogels for repeated mechanical deformation in bioelectronic applications.

3.2. Electrical and electrochemical evaluation of the hydrogels

The electrical conductivity of the hydrogels varied significantly depending on the type and concentration of the conducting polymer added (Fig. 4). Pristine Alg–GEL exhibited negligible conductivity ($<10^{-5}$ S cm^{-1}), consistent with its insulating nature.

Adding PEDOT:PSS resulted in an apparent increase, with conductivity gradually rising from PEDOT4 to PEDOT10. The highest value among PEDOT-only samples approached $\sim$0.1 S × cm^{-1}, aligning with reported values for highly hydrated PEDOT-based composites in the literature.[42,43] This increase is attributed to the formation of interconnected PEDOT:PSS domains, which facilitate efficient electronic transport through the otherwise insulating hydrogel matrix.

In situ polymerization of PPy within Alg–GEL produced even higher conductivity than PEDOT alone, despite similar polymer loadings. This indicates that PPy forms extensive, percolating networks within the hydrogel pores, creating continuous pathways for electrons. Notably, conductivity values reached $\sim$1.8 S × cm^{-1}, which is high for soft, water-rich hydrogels.

The hybrid systems combining PEDOT:PSS and PPy exhibited the highest overall conductivities. Specifically, the Alg–GEL–Py0.1–PEDOT10 sample achieved around $\sim$3.7 S × cm^{-1}, nearly two orders of magnitude higher than the PEDOT-only-based Alg–GEL hydrogel. This synergistic effect likely results from complementary conduction pathways: PEDOT:PSS ensures a uniform distribution of conductive domains, while PPy polymerization creates interconnected, rigid conductive clusters that together form a dense percolation network. These values place the developed hydrogels among the best-performing electroconductive hydrogels reported to date, greatly surpassing many alginate- or gelatin-based systems that usually stay below 10^{-2}–10^{-3} S cm^{-1}[16,42,43]. Moreover, such conductivity levels are sufficient to support the charge transfer processes required for neural stimulation and electrophysiological signal recording, as demonstrated by conductive hydrogel coatings that significantly lower electrode impedance and enhance charge injection capacity in neural electrode studies.[44]

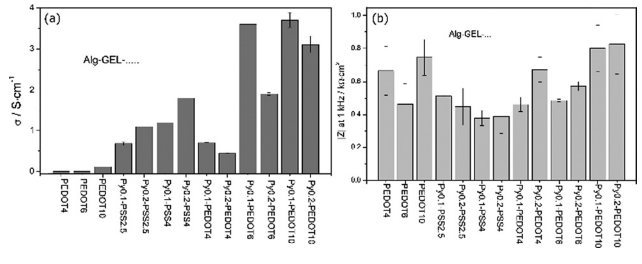

Fig. 4 Electrical conductivity (a) and interfacial impedance |*Z*| at 1 kHz (b) of the hydrogels.

Impedance is a crucial electrochemical parameter of bioelectrodes, as it influences both the efficiency of neural stimulation and the quality of electrophysiological recordings. Specifically, impedance measured at 1 kHz is commonly used as a standard reference because this frequency falls within the spectral range of neural action potentials and directly influences the signal-to-noise ratio and the charge injection capacity of electrodes.[45] Consequently, we measured the impedance of all hydrogel formulations, and the values determined at 1 kHz are shown in Fig. 4b.

PEDOT:PSS-containing hydrogels showed impedance values in the lower kΩ cm^2 range, indicating efficient charge transport and increased interfacial capacitance due to the conducting polymer. Hydrogels with *in situ* polymerized PPy within the Alg–GEL network also demonstrated reduced impedance, with the extent of reduction depending on the pyrrole concentration. Samples containing *in situ* polymerized PPy (PSS-doped) showed the lowest impedance values among all groups, especially at higher pyrrole/dopant concentrations (*e.g.*, Alg–GEL–Py0.1–PSS4 $\sim$ 0.4 kΩ cm^2), indicating the formation of an efficient, ionically accessible conducting network. Hybrid formulations combining PEDOT:PSS and PPy yielded impedances comparable to or higher than those of the best PPy-only systems. Notably, Alg–GEL–Py0.1–PEDOT10 did not show the lowest impedance ($\sim$0.8 kΩ cm^2), despite having the highest bulk electrical conductivity among all samples (Fig. 4a).

These differences show that impedance at 1 kHz depends not only on bulk conductivity but also on microstructural and interfacial effects, including ion mobility, double-layer capacitance, and the continuity of conducting domains. *In situ* PPy networks, especially with PSS doping, increase effective interfacial area and capacitance while providing electronic pathways, resulting in lower impedance. In hybrid systems, phase segregation and the highly hydrated nature of PSS probably introduce additional resistive or dispersive components, preventing further impedance reduction beyond that of the optimized PPy-only samples.

To further support these observations, full impedance spectra recorded over a wide frequency range (0.1 Hz–10 kHz) are provided in the Supplementary Materials (Fig. S6). At lower frequencies, the impedance response is increasingly influenced by ionic diffusion and electrode polarization, whereas at higher frequencies the spectra converge, indicating bulk and interfacial charge-transport processes. Although frequency-dependent differences between formulations are apparent, the relative ranking of the hydrogels remains consistent with the impedance values obtained at 1 kHz. This confirms that impedance at 1 kHz is a representative and practical metric for comparing the electrochemical performance of soft hydrogel bioelectrodes.

To further assess the electrical properties, impedance values at 1 kHz were compared with the hydrogels' bulk conductivities (Fig. S7, SI). A clear inverse relationship was observed: samples with higher conductivity exhibited lower impedance. However, this relationship was not strictly linear. Formulations containing *in situ* polymerized PPy, particularly the PEDOT–PPy hybrids, showed significantly lower impedance than predicted by their bulk conductivities alone. This difference suggests that other transport mechanisms also contribute to charge transfer within these systems. First, PPy-rich regions enhance ion mobility in the hydrogel by creating hydrated, ion-permeable channels, which have been shown to lower impedance independently of electronic conductivity.[46,47] Second, granular PPy and PEDOT regions increase the effective interfacial capacitance by expanding the electrochemically active surface area, which reduces impedance at 1 kHz through improved double-layer and pseudocapacitive charging.[30,48] Third, synergistic transport at PEDOT–PPy–biopolymer junctions creates mixed ionic–electronic percolation pathways, discussed in the literature for composite conducting polymer hydrogels, that enable more efficient charge compensation and decrease interfacial resistance.[49,50]

To evaluate the redox properties and electrochemical stability of the developed hydrogels, cyclic voltammetry (CV) was performed (Fig. 5).

CV analysis provides insights into faradaic charge storage, capacitive behavior, and the electrochemical stability window, key parameters for the safety and efficiency of materials used in neural bioelectrodes.[51] Therefore, to determine the electrochemical stability window, CV measurements were intentionally conducted over an extended potential range (−1.2 to +1.2 V *vs.* Ag/AgCl), enabling precise identification of the onset of water redox reactions. PEDOT-modified hydrogels (Alg–GEL–PEDOT4, Alg–GEL–PEDOT6, and Alg–GEL–PEDOT10) mainly showed capacitive current responses with broad, featureless faradaic contributions typical of PEDOT (Fig. 5a). During the cathodic sweep (from about 0 V to −1.2 V), a sharp increase in negative current occurs near the most negative potentials, primarily due to water oxidation; during the anodic sweep, a broad positive feature appears around −0.8 to −0.5 V (*vs.* Ag/AgCl$_{sat}$), followed by a low current plateau indicating PEDOT p-doping/de-doping accompanied by double-layer charging.[52] The overall current varied among samples, with Alg–GEL–PEDOT6 showing the highest current density, followed by PEDOT4 and PEDOT10. Notably, the hydrogels' accessible potential window was broader than that of conventional PEDOT thin films.[53] While PEDOT coatings usually undergo water oxidation at anodic potentials above approximately +0.6 V *vs.* Ag/AgCl, no such process was observed in the PEDOT-hydrogel composites within the tested anodic range (up to +1.2 V). On the cathodic side, water reduction began at around −0.70 V for PEDOT6, −0.75 V for PEDOT4, and −0.85 V for PEDOT10. Therefore, within the tested potential range, PEDOT-containing hydrogels exhibited an extended electrochemical stability window compared to standard PEDOT:PSS films. This behavior is highly beneficial for bioelectrode applications, as it reduces the risk of water electrolysis and allows for higher safe charge injection during neural stimulation.

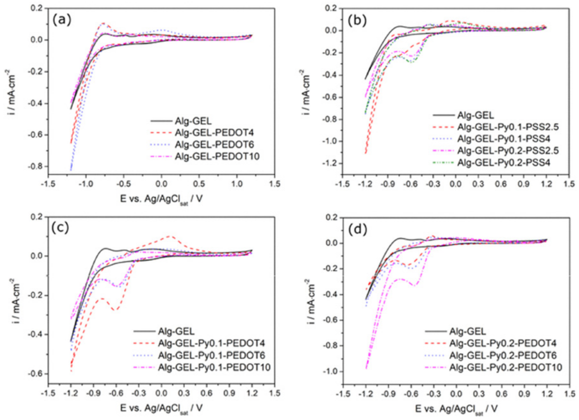

Fig. 5 Cyclic voltammograms of the hydrogels (a–d) recorded in a wide potential range.

Cyclic voltammetry performed on the PPy/PSS-containing hydrogels showed a much stronger electrochemical response compared to PEDOT-based systems (Fig. 5b). Along with the capacitive background current typical of hydrated hydrogel matrices, distinct redox peaks appeared at about −0.35 V (oxidation) and −0.60 V (reduction), which can be attributed to the electroactivity of polypyrrole–PSS domains. Similar features have been observed in PPy–PSS films.[54] The presence of these peaks confirms the successful *in situ* polymerization of polypyrrole and its effective doping by PSS, creating redox-active sites spread throughout the Alg–GEL network.

Notably, the intensity of the reduction peak increased with higher PSS content, indicating that the polyanionic dopant not only stabilizes the oxidized PPy backbone but also promotes greater charge compensation during the redox cycle. This effect demonstrates a stronger interaction between the polymeric dopant and the conducting domains, effectively adjusting the system's redox capacity. The redox behavior was observed within a relatively broad electrochemical window, as water oxidation was not visible within the studied potential range, and water reduction occurred only at potentials below approximately −0.7 V, depending on the formulation.

Overall, these results highlight the complementary benefits of PPy–PSS domains over PEDOT:PSS inclusion: while PEDOT mainly helps to reduce impedance and increase electronic conductivity, PPy–PSS provides unique and adjustable faradaic processes that can enhance the charge storage and modulation ability of the hydrogel electrodes. This dual function demonstrates that adjusting the PPy-to-PSS ratio is an effective way to balance capacitive and faradaic charge transfer mechanisms in soft, hydrogel-based bioelectrodes.

To better explain the redox properties of the hybrid hydrogels, CV measurements were performed on formulations containing both PEDOT and *in situ* polymerized PPy (Fig. 5c-d). In the hybrids with low pyrrole content (Py0.1), the electrochemical response was primarily dominated by PEDOT, and the characteristic PPy–PSS oxidation peak, located around −0.3 to

−0.4 V, was not readily visible. This suggests that the PEDOT regions primarily control charge storage and may partially obscure PPy's redox activity. However, the cathodic region showed significant reduction currents, consistent with the presence of PSS throughout the network, which encourages ion exchange and enhances capacitive behavior.

When the pyrrole concentration was increased to 0.2 M, the PPy–PSS oxidation feature became visible, especially in the PEDOT4 hybrid, confirming the presence of both conducting polymer phases. However, at higher PEDOT contents (6 and 10), this oxidation signal was diminished, likely because it overlapped with the broad PEDOT redox processes. In all hybrid systems, the reduction processes were prominent, highlighting the synergistic role of PEDOT, PPy, and PSS in stabilizing ionic transport and improving charge injection capacity. These results demonstrate that the PEDOT:PPy ratio is crucial in shaping the redox signature of the hybrids, with PEDOT-rich systems showing smoother profiles and higher-pyrrole formulations exhibiting more complex redox features.

Overall, the CV analysis emphasizes the complementary roles of PEDOT and PPy within the hydrogel matrix. Pure PEDOT-containing samples showed wide potential windows and smooth capacitive profiles, indicating stable charge storage. In contrast, PPy–PSS systems exhibited distinct redox peaks characteristic of polypyrrole, indicating more localized electron-transfer processes. The hybrid hydrogels combined the features of both polymers: PEDOT-dominated formulations (with low pyrrole content) maintained the broad, stable PEDOT response. In contrast, higher pyrrole concentrations introduced additional PPy-related redox activity. These findings demonstrate that adjusting the PEDOT–PPy ratio modulates redox behavior, balancing capacitive stability and faradaic contributions in soft hydrogel bioelectrodes.

To assess the stimulation performance of the hydrogels, 1 ms biphasic current pulse tests were conducted to determine the current injection limit (CIL). The CIL was defined as the highest current amplitude that keeps the electrode potential within the water-stable window as determined by CV. The main manuscript presents representative results for the best-performing samples from each hydrogel group (Fig. 6a–c), alongside a commercial Pt electrode for comparison (Fig. 6d). Additionally, CIL values for all formulations are provided in the SI (Fig. S8).

PEDOT-only hydrogels (PEDOT4/6/10) consistently supported the highest CIL (4.0 mA), despite their modest bulk conductivities for PEDOT4/6. This apparent discrepancy is explained by the large accessible potential window observed in CV, with no anodic water oxidation beyond +1.2 V and a delayed cathodic reduction onset (∼−0.70 to −0.85 V). Conversely, PPy/PSS formulations exhibited lower CIL values (1.0–2.0 mA) despite their relatively low impedances and high bulk conductivities, indicating that CIL is mainly governed by interfacial electrochemical stability and transient charge transfer kinetics rather than σ or $|Z|$ at 1 kHz. Hybrid PEDOT + PPy samples fell in between (0.5–2.0 mA); notably, systems combining high PEDOT content (PEDOT10) with PPy showed the lowest CIL (*e.g.*, Py0.1–PEDOT10 = 0.5 mA), consistent with CV evidence of overlapping PEDOT/PPy redox features and earlier cathodic excursions that narrow the safe stimulation window.

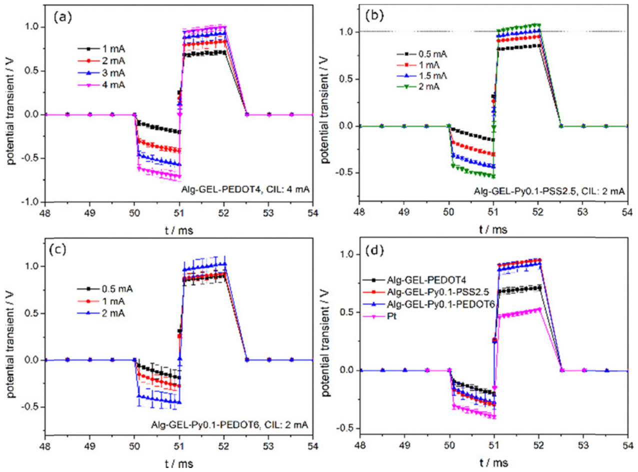

Fig. 6 Potential response of Alg–GEL–PEDOT4 (a), Alg–GEL-Py0.1-PSS2.5 (b), and Alg–GEL-Py0.1-PEDOT6 (c) to the biphasic current pulse of 0.5/1-2/4 mA. Comparison of the potential response of selected hydrogels and platinum (Pt) electrode to the biphasic current pulse of +/− 1 mA (d).

To establish a benchmark, we compared the voltage transients at 1 mA stimulation for the best-performing hydrogel from each group with a commercial platinum electrode (Fig. 6d). The Alg–GEL–PEDOT4 sample exhibited the lowest potential excursion among all hydrogels, closely matching that of Pt. Although platinum exhibited slightly lower anodic excursions, the difference was moderate; on the cathodic side, however, PEDOT-based hydrogels clearly outperformed Pt, showing significantly smaller voltage drops. This suggests fewer parasitic faradaic reactions and a more capacitive charge injection process in the hydrogel systems.

Overall, these findings emphasize that maximizing CIL involves tuning the electrochemical stability window and interfacial charge transfer pathways, rather than relying solely on bulk conductivity or impedance. Importantly, PEDOT hydrogels exhibit charge-injection capabilities superior to those of PPy systems and competitive with platinum, highlighting their potential as safe and efficient soft electrodes for neural stimulation.

To assess the pre-liminary electrochemical stability and interfacial robustness of the developed hydrogels, representative formulations (Alg–GEL, Alg–GEL–PEDOT6, Alg–GEL–Py0.1–PSS2.5, and Alg–GEL–Py0.1–PEDOT6) underwent repeated cyclic voltammetry (100 cycles), followed by impedance spectroscopy recorded before and after cycling (Fig. S9 and S10). The cycling potential range (−0.6 to +0.6 V *vs.* Ag/AgCl$_{\text{sat}}$) was chosen based on the electrochemical stability window identified from wide-range CV measurements (Fig. 5), ensuring that the repeated cycling tests stay entirely within the safe operational limits of the hydrogels.

For Alg–GEL, PEDOT6, and Py0.1–PSS2.5, the impedance spectra remained essentially unchanged throughout the entire frequency range studied (10 kHz–0.1 Hz), indicating stable ion and electron transport pathways and a preserved electrode–electrolyte interface within the cycling window. In contrast, the hybrid Alg–GEL–Py0.1–PEDOT6 showed more significant changes after cycling, particularly in the mid-frequency range (∼100–1000 Hz), which is often associated with interfacial and capacitive effects. Consistently, the cyclic voltammograms revealed a gradual reduction in hysteresis with increasing cycle number, indicating a partial decrease in reversible charge storage. This behavior is due to the coexistence of PEDOT-dominated capacitive domains and PPy-rich faradaic regions within the hybrid network, where repeated polarization can lead to interfacial conditioning and a redistribution of charge-storage contributions. Importantly, no sudden increase in impedance, loss of electrochemical activity, or narrowing of the accessible potential window was observed for any formulation.

Overall, these results show that the developed hydrogels keep stable electrochemical performance during repeated polarization, with hybrid systems exhibiting mild conditioning effects rather than degradation. The maintained impedance levels and characteristic CV shapes confirm the strength of the conducting polymer networks and support their suitability for bioelectronic applications that require repetitive electrical stimulation or recording.

3.3. Swelling and wet-mass-retention study of the hydrogels

The swelling of the developed hydrogels was examined by monitoring their wet weight over an incubation period of up to 28 days (Fig. 7).

For all tested hydrogel compositions, an initial swelling was observed, followed by only slight weight changes, indicating that the hydrogels showed no signs of degradation. During the first 24 hours of incubation, Alg–GEL–PEDOT hydrogels exhibited an increased swelling capacity with higher PEDOT concentrations, reaching maximum swelling of 41 ± 20%, 52 ± 14%, and 56 ± 7% for Alg–GEL–PEDOT4, –PEDOT6, and –PEDOT10 after 24 hours, respectively. Additionally, PEDOT-modified hydrogels exhibited greater swelling than the reference Alg–GEL, reaching 37 ± 4% after 24 hours.

A similar pattern was observed for PPy-modified hydrogels, which displayed prolonged swelling up to 7 days of incubation, by which time the hydrogels had achieved their maximum swelling values. Furthermore, comparing polypyrrole-only modified hydrogels with PEDOT-modified ones reveals that PPy-modified samples swelled more, reaching swelling values of up to 97 ± 5% for Alg–GEL–Py0.1–PSS4. Moreover, higher PSS concentrations resulted in greater swelling when the polypyrrole content was held constant. For the hybrid hydrogels, the modified samples again swelled more than pristine Alg–GEL, reaching their peak swelling after 7 days. It was noted that Py0.2 samples showed greater swelling and greater stability over the 28-day incubation period than their Py0.1 counterparts.

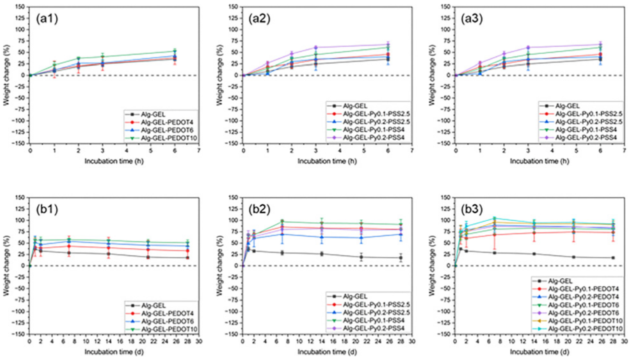

Fig. 7 Weight change of samples over incubation time in DMEM within the first 24 h (a1)–(a3) and up to 28 days (b1)–(b3) under cell culture conditions.

Additionally, increasing the PEDOT concentration was correlated with higher swelling and enhanced long-term stability. Overall, the conductive polymer-modified samples demonstrated improved long-term stability compared to pristine Alg–GEL, which showed a decrease in weight over 28 days. The increased swelling of PEDOT:PSS- or PPy:PSS-modified hydrogels is attributable to the hydrophilic nature of the conductive polymer, particularly the dopant PSS. Polystyrene sulfonate strongly attracts water molecules, thereby increasing osmotic pressure and resulting in higher swelling ratios. Conversely, the improved long-term stability results from the formation of an interpenetrating polymer network, in which the conductive polymer is entangled within the hydrogel, thereby forming additional physical crosslinks. This enhances structural integrity by creating a barrier that prevents alginate or gelatin from leaching out or disentangling, thereby contributing to greater long-term stability.

3.4. Investigation of cell material interactions with NIH3T3 fibroblast cells

The cytocompatibility of alginate-gelatin-based hydrogels was examined by seeding NIH3T3 fibroblast cells on the freshly prepared hydrogels. Cell activity of the seeded cells was measured using a WST-8 assay (Fig. 8a).

All hydrogels supported the attachment and proliferation of NIH3T3 fibroblasts with only minor differences between the groups after one day of incubation. However, after seven days, PPy- and PPy–PEDOT-modified hydrogels showed higher absorbance values than the unmodified Alg–GEL. In contrast, Alg–GEL–PEDOT samples exhibited similar or lower values compared to the control. Overall, a trend of increased cell activity with higher polypyrrole molarity was observed. In addition to the WST-8 assay, cells were stained with Calcein-DAPI and imaged *via* fluorescence microscopy to assess their morphology (Fig. 8b).

After seven days, cells were present on all hydrogels, but the modified hydrogels had a higher number of attached and spread fibroblasts. When comparing the modified hydrogels, the Alg–GEL–PEDOT samples contained fewer cells than the PPy-only or PPy–PEDOT-modified Alg–GEL samples, confirming the WST-8 results. Generally, as seen in the WST-8 assay, higher polypyrrole molarity was correlated with a greater number of attached cells. The cytocompatibility of alginate–gelatin-based hydrogels with various cell types, including fibroblasts,[55] bone cells,[56] and neural cells,[57] has been extensively demonstrated.

Additionally, the literature confirms that polypyrrole and PEDOT are biocompatible conductive polymers.[58] Our findings support the biocompatibility of all the developed hydrogels and

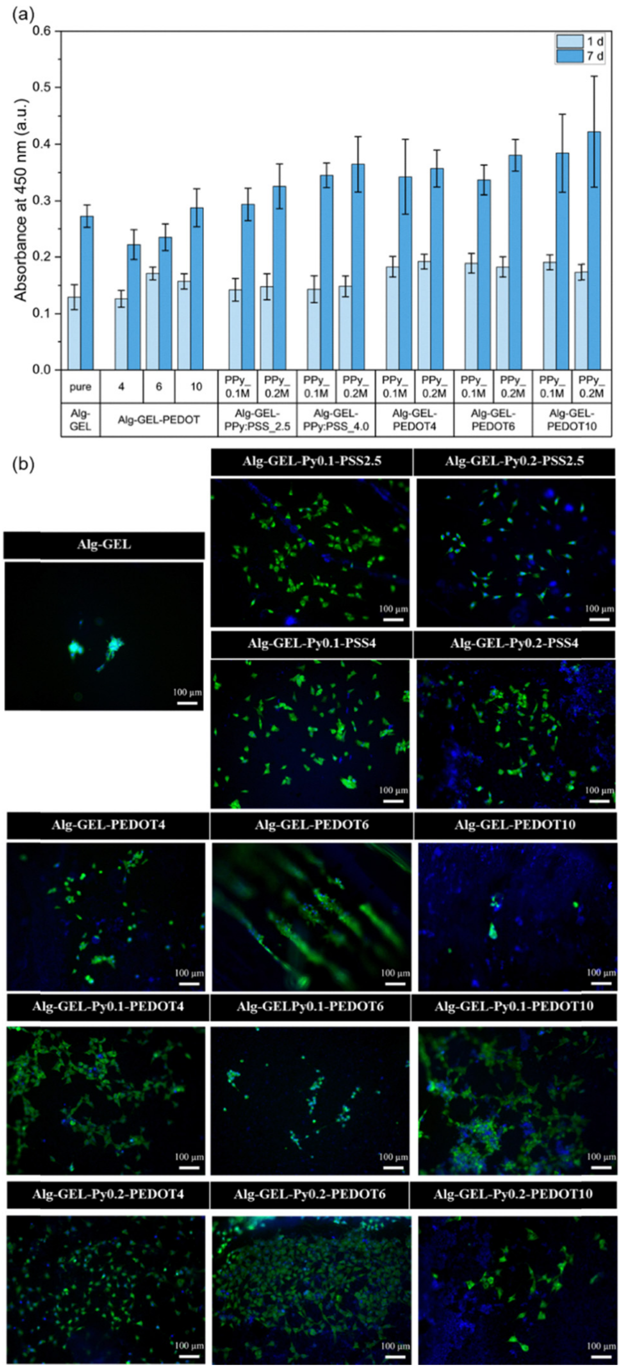

Fig. 8 Investigation of cell-material interactions with NIH3T3 cells by WST-8 assay (a) and (b) Calcein-DAPI staining after 7 days of culture. Scale bar = 100 μm.

suggest that combining these two conductive polymers can enhance cytocompatibility compared to using polypyrrole or PEDOT alone. Therefore, it can be concluded that the hydrogels are cytocompatible and have potential for use as safe neural probes.

The systems listed in Table 1 were chosen based on two criteria: (i) they represent recent state-of-the-art hydrogel electrodes that incorporate well-established conducting polymers (such as PEDOT, PEDOT:PSS, PPy, or their variants), and (ii) they serve as functional benchmarks relevant to neural recording and stimulation, where conducting polymers are the current gold-standard materials. While not limited to Alg–GEL matrices, these studies provide the closest functional benchmarks available for comparison with the current work.

Quantitative comparison with previously reported conductive hydrogel electrodes shows that the developed Alg–GEL–PEDOT/PPy systems are among the top performers of soft electroactive materials. Most PEDOT-based hydrogels reported in the literature have electrical conductivities ranging from 10^{-3} to 10^{-1} S cm^{-1}, elastic moduli between 10 and 600 kPa, and current injection limits usually below 1–2 mA. In contrast, the current formulations achieve conductivities up to 3.7 S cm^{-1} while maintaining tissue-like mechanical properties (50–60 kPa). Additionally, the hydrogels feature an exceptionally wide electrochemical stability window, with no signs of anodic water oxidation up to +1.2 V, and support high current injection limits of up to 4 mA. Overall, these features rank the developed materials among the highest-performing PEDOT- or PPy-based soft hydrogel electrodes reported so far, as summarized in Table 1.

A direct correlation was observed between the microstructure revealed by SEM and the electrochemical behavior of the hydrogels. The gradual densification of PEDOT, progressing from fibrous surface deposits (PEDOT4) to cauliflower-like granular domains (PEDOT6) and finally to dense, thick-walled structures (PEDOT10), formed increasingly continuous electronic percolation pathways. These dense PEDOT-rich networks enabled efficient electronic transport through the hydrogel. They reduced tortuosity to facilitate ionic migration, explaining both the steady rise in bulk conductivity and the expansion of the electrochemical stability window observed in CV. Dense, PEDOT-dominated areas also reduced localized redox sites, resulting in smooth, capacitive-like CV curves and delayed water reduction, supporting the high current injection limits (CIL = 4 mA) despite only moderate bulk conductivity.

In contrast, PPy/PSS-containing hydrogels exhibited microstructures with granular, fibrillar, and vein-like surface features, which directly led to discrete oxidation–reduction peaks in CV. These granular PPy–PSS clusters serve as ''redox islands'' that store and release charge through faradaic processes, significantly boosting conductivity and charge storage capacity. However, the same discrete redox centers also cause earlier redox activity at negative potentials, narrowing the usable electrochemical window and limiting CIL (1–2 mA). The rougher, more heterogeneous morphologies observed at higher pyrrole or PSS concentrations further increased the effective interfacial area and ionic accessibility, explaining the very low impedance values of the PPy samples, even when the bulk conductivity did not explicitly predict them.

Hybrid PEDOT–PPy hydrogels showed an intermediate, composition-dependent behavior, reflecting the coexistence of two structurally and functionally different conductive phases. When PEDOT was the dominant component, the morphology remained compact and smooth, stabilizing the potential window but partially masking PPy's redox activity. Increasing pyrrole content introduced granular, PPy-rich domains within

Table 1 Hydrogel systems and their electrical and mechanical properties have recently been reported in the literature

Type of hydrogel	Fabrication	Young's modulus	σ	$\|Z\|$	Ref.
PEDOT:P(SS-coNHMAA) + PEG200	Chemical polymerization/3D printing (PDMS)	4–20 MPa	—	30.0 Ω (10 Hz) 28.0 Ω (1 kHz)	59
PEDOT:PSS–PVA–PAA–NHS–CTS–GA	3D printing – direct ink writing (PET, PDMS, carbon cloth)	$\sim$1.5 MPa	—	20 Ω (10 Hz & 1kHz)	60,61
PEDOT:PSS in ionic liquid (4-(3-butyl-1-imidazolio)-1-butanesulfonic acid trifate)	Spin-coating (PFPE-DMA)	$\sim$24–32 kPa	—	1 kΩ cm^2 (10 Hz) 900 Ω cm^2 (1 kHz)	61
PEDOT:PSS-DMSO	Chemical, drop-casting of ink on PET foil	$\sim$2 MPa	20 S × cm^{-1} in PBS	—	62
PEDOT:PSS-Pln5-NH_2	Chemical polymerization, drop-casting	$\sim$200 Pa	33 S × cm^{-1}	—	20
PEDOT:PSS-LcP (light curing polymer)-Irgacure	Photolithography, conductive path on flexible substrates	$\sim$10 kPa	$\sim$20 S × cm^{-1} (high PEDOT:PSS content, $\sim$30 wt%)	$\sim$40 Ω (1 kHz), no information about surface area	21
PEDOT:PSS–alginate	Chemical synthesis	$\sim$0.4 GPa	$\sim$14 mS × cm^{-1}	R_{sheet} $\sim$3.5 Ω sq^{-1}	42
PEDOT–PVA–PAM stretchable	Chemical synthesis, 3D printable	$\sim$kPa	0.32 S cm^{-1}	—	22
PEDOT-gelatin methacryloyl/chitosan	Chemical polymerization, 3D printable	$\sim$2 MPa	$\sim$10 mS × cm^{-1}	$\sim$8 Ω cm^2	63
Alg–GEL–CNFs	Chemical synthesis, 3D printable	$\sim$500 kPa	0.4 mS × cm^{-1}	—	43
Alg–GEL–PPy	*In situ* polymerization	$\sim$40–58 kPa	0.6–1.8 S × cm^{-1}	0.4–0.5 kΩ cm^2	This work
Alg–GEL–PEDOT	Blending	$\sim$5–10 kPa	0.1–0.3 S × cm^{-1}	0.45–0.75 kΩ cm^2	This work
Alg–GEL–PPy–PEDOT	Blending, and *in situ* polymerization	$\sim$40–70 kPa	0.5–3.7 S × cm^{-1}	0.45–0.8 kΩ cm^2	This work

the PEDOT matrix, resulting in more complex surfaces with a mix of compact and fibrillar features. These hybrid microstructures supported simultaneous capacitive (PEDOT-driven) and faradaic (PPy-driven) charge transfer. Still, the overlap between these processes led to earlier redox excursions, reducing CIL, especially in PEDOT10-based hybrids, where dense PEDOT domains interacted with dispersed PPy aggregates. This explains why hybrids with the highest conductivity (*e.g.*, Py0.1–PEDOT10, $\sim$3.7 S cm^{-1}) did not have the lowest impedance or the highest CIL.

Overall, these structure–function relationships indicate that: (i) compact PEDOT-rich morphologies favor wide stability windows, low anodic excursions, and high safe stimulation currents; (ii) granular PPy/PSS morphologies enhance faradaic charge storage and decrease impedance but limit the electrochemical window; (iii) hybrid morphologies allow adjustable combinations of these behaviors but require careful balancing of compact PEDOT networks and PPy granular domains to prevent overlapping redox limitations.

These findings highlight that the microstructural organization of conducting polymers within the hydrogel, not just their concentration, determines the balance between capacitive and faradaic charge transfer, electrochemical stability, and ultimately the performance of soft hydrogel bioelectrodes.

This structure–function relationship is also evident in the interaction between mechanical stiffness and electrical conductivity (Fig. S11). When plotting Young's modulus against bulk conductivity, a wide scatter appears instead of a single pattern, showing that electrical performance is not just controlled by mechanical strength. PEDOT-rich systems have relatively low modulus and moderate conductivity, while PPy-containing and hybrid hydrogels tend to be stiffer and reach conductivities in the S cm^{-1} range. Notably, hybrid formulations span a wide range of properties, demonstrating that conductivity and stiffness can be adjusted independently through microstructural design. This separation of mechanical and electrical traits is essential for neural biointerfaces, where tissue-like softness must be preserved without compromising charge transport or stimulation.

Adding PEDOT and PPy also impacted the hydrogel's stability. Pristine Alg–GEL gradually lost weight over 28 days. In contrast, hydrogels modified with conducting polymers maintained their structural integrity, consistent with the formation of interpenetrating networks in which PEDOT and PPy domains serve as additional crosslinks. Meanwhile, both PEDOT:PSS- and PPy:PSS-containing samples showed significantly higher swelling ratios due to the strong hydration tendencies of PSS, which uses sulfonate groups to attract water and partially weaken Ca^{2+}–alginate ionic junctions. Notably, these swelling measurements (*e.g.*, 56 ± 7% for PEDOT10, 97 ± 5% for Py0.1-PSS4) provide a quantitative estimate of each formulation's hydration level. This aligns with the mechanical results: samples with higher PSS content displayed slightly lower Young's modulus despite increased polymer loading, indicating that PSS-driven hydration and network plasticization partially counteract the stiffening effect of PPy or PEDOT domains. Therefore, even without dedicated gravimetric hydration tests, the swelling behavior observed in the long-term stability study supports the proposed mechanism, which states that increased hydration at higher dopant levels contributes to the observed softening.

Overall, the results of this study show that the performance of Alg–GEL hydrogels modified with PEDOT:PSS, PPy/PSS, and their hybrids depends on a combination of their mechanical, electrical, and electrochemical properties rather than any single factor. While polymer loading affects both bulk conductivity and stiffness, neither property alone predicts electrochemical stability or stimulation tolerance. PEDOT-rich morphologies uniquely extend the electrochemical stability window and support high, safe stimulation currents, achieving performance comparable to that of platinum electrodes. In contrast, PPy/PSS enables reversible faradaic charge storage, significantly reducing impedance but narrowing the operational potential range. Hybrid PEDOT–PPy systems combine these behaviors in a tunable way; however, their performance relies on maintaining a proper balance between compact PEDOT domains and granular PPy regions to prevent overlapping redox processes. Although adding conducting polymers increases swelling due to the hydrophilic PSS dopant, it also improves long-term structural stability by forming interpenetrating polymer networks that prevent Alg–GEL leaching. Ultimately, all hydrogels demonstrated cytocompatibility, with hybrid formulations supporting especially favorable cell–material interactions.

In practical bioelectronic translation, it is crucial to examine how developed materials overcome the limitations of existing clinical electrode technologies. State-of-the-art neural electrodes used in deep brain stimulation, cortical recording, and peripheral neuromodulation are usually made from platinum or platinum–iridium (Pt–Ir) alloys. Although these metals offer excellent electrical conductivity, their high stiffness ($E \approx$ 160–170 GPa) creates a significant mechanical mismatch with soft neural tissue ($E \approx$ 0.1–10 kPa), leading to chronic inflammation, glial encapsulation, micro-motion–related injury, and long-term signal loss.[64,65] Furthermore, metal electrodes depend on redox reactions at their interface, which limits safe charge injection and leads to instability during long-term stimulation.

The hydrogel systems developed here directly address these challenges. Their inherent softness ($E \approx$ 8–60 kPa) and high hydration enable the formation of a mechanically compatible interface that can significantly reduce the foreign body response compared to rigid metal electrodes. PEDOT-rich formulations, with broader electrochemical stability windows and higher current injection limits, are well-suited as soft conductive coatings that can be conformally applied onto existing Pt/Pt-Ir microelectrodes to improve biocompatibility and electrochemical performance. Hybrid PEDOT–PPy systems, which offer adjustable faradaic and capacitive behaviors, may further expand the functions of implantable sites.

From a fabrication perspective, the precursor solutions used here can be cast into microstructured wells, drop-cast onto metal microelectrodes, or formulated for extrusion-based or inkjet 3D printing. This creates a clear pathway toward patterned hydrogel interfaces on flexible substrates (PDMS, parylene-C, polyimide) and eventually toward fully hydrogel-only electrodes, where the conducting polymer network replaces the metallic current collector. Recent demonstrations of printable conductive polymer hydrogels support the feasibility of this approach. With further optimization of the ink rheology and crosslinking kinetics, the formulations reported here could be adapted for high-resolution additive manufacturing of custom neural probes for recording or stimulation.

Together, these considerations outline a practical translational pathway: (i) use hydrogels as soft coatings to enhance the performance and compatibility of existing metal electrodes; (ii) integrate them onto flexible substrates to develop minimally invasive soft microelectrodes; (iii) eventually, produce metal-free, fully hydrogel-based electrodes through 3D printing once the mechanical, electrical, and stability requirements are fully optimized.

4. Conclusions

Conductive hydrogels based on Alg–GEL modified with PEDOT:PSS, PPy/PSS, and their hybrids were successfully developed and thoroughly characterized. The results suggest that hydrogel performance results from the combined influence of mechanical, electrical, and electrochemical properties rather than from any single factor. Incorporating PEDOT strengthened the hydrogel network and expanded the electrochemical stability window, enabling high current injection (up to 4 mA). Adding PPy provided additional reversible redox activity and increased charge storage, although it also narrowed the stable potential window. Hybrid formulations offered adjustable combinations of these features, with performance closely tied to the PEDOT-to-PPy ratio. SEM, FTIR, and EDX analyses confirmed the successful integration and uniform distribution of conductive polymer domains within the Alg–GEL matrix. The incorporation of conductive polymers also improved long-term stability, attributed to the formation of an interpenetrating network, while maintaining cytocompatibility across all formulations. The hybrid systems exhibited the most favorable cellular responses. Compared to platinum, PEDOT-based hydrogels demonstrated competitive anodic behavior and superior cathodic performance, while also possessing mechanical properties similar to those of natural tissue. Overall, the study suggests that PEDOT- and PPy-modified hydrogels offer a versatile and promising platform for next-generation soft neural interfaces, where safe charge injection, long-term stability, and biocompatibility are crucial.

Author contributions

The manuscript was written through the contributions of all authors. All authors have approved the final version of the manuscript. K. C.: conceptualization, writing and review, investigation (hydrogel fabrication, electrical and electrochemical studies, cytotoxicity tests, SEM/EDX and FTIR analysis, data analysis, visualization; L. S.: writing and review, investigation (hydrogel fabrication, cytotoxicity studies, swelling studies), visualization, data analysis, statistics; A. R. B.: conceptualization, writing, review and editing, resources, supervision, project administration, funding acquisition.

Conflicts of interest

There are no conflicts to declare.

Data availability

The experimental data are available in the MOST Wiedzy Repository at Gdansk University of Technology, with the corresponding DOI: https://doi.org/10.34808/4vha-1p33. The supplementary information includes additional results obtained within this work.

The data supporting this article have been included as part of the supplementary information (SI). Supplementary information is available. See DOI: https://doi.org/10.1039/d5tb02148k.

Acknowledgements

The work was supported by the KMM-VIN Mobility Programme 2023. Thanks, Grammarly program, for English corrections.

Notes and references

1 Y. Huang, K. Yao, Q. Zhang, X. Huang, Z. Chen, Y. Zhou and X. Yu, *Chem. Soc. Rev.*, 2024, **53**, 8632–8712.
2 J. Rivnay, R. Raman, J. T. Robinson, C. Schreib, T. Cohen-Karni, K. E. Galloway and O. Veiseh, *Nat. Rev. Bioeng.*, 2025, **3**, 317–332.
3 S. H. Sunwoo, S. I. Han, C. S. Park, J. H. Kim, J. S. Georgiou, S. P. Lee, D. H. Kim and T. Hyeon, *Nat. Rev. Bioeng.*, 2023, **2**, 8–24.
4 S. Gong, Y. Lu, J. Yin, A. Levin and W. Cheng, *Chem. Rev.*, 2024, **124**, 455–553.
5 M. Kim, H. Lee, S. Nam, D. H. Kim and G. D. Cha, *Acc. Chem. Res.*, 2024, **57**, 1633–1647.
6 D. Boufidis, R. Garg, E. Angelopoulos, D. K. Cullen and F. Vitale, *Nat. Commun.*, 2025, **16**, 1–17.
7 S. Cheng, R. Zhu and X. Xu, *Commun. Mater.*, 2024, **5**, 1–9.
8 T. Basu, U. Bhutani and S. Majumdar, *J. Mater. Chem. B*, 2022, **10**, 3614–3623.
9 R. A. ElTatawy, A. M. Ismail, M. S. Ayoup, M. M. F. Ismail and H. A. Fetouh, *Sci. Rep.*, 2024, **14**, 1–18.
10 L. Wang, H. J. Zhang, X. Liu, Y. Liu, X. Zhu, X. Liu and X. You, *ACS Appl. Polym. Mater.*, 2021, **3**, 3197–3205.
11 Z. Chen, C. Xu, X. Chen, J. Huang and Z. Guo, *Small Methods*, 2025, **9**, 2401156.
12 H. Li, J. Cao, R. Wan, V. R. Feig, C. M. Tringides, J. Xu, H. Yuk and B. Lu, *Adv. Mater.*, 2025, **37**, 2415151.
13 R. E. Daso, R. Posey, H. Garza, A. Perry, C. Petersen, A. C. Fritz, J. Rivnay and J. Tropp, *Adv. Funct. Mater.*, 2025, **35**, e08859.
14 P. S. Floris, C. Melis and R. Rurali, *Adv. Funct. Mater.*, 2023, **33**, 2215125.
15 A. L. Pang, A. Arsad and M. Ahmadipour, *Polym. Adv. Technol.*, 2021, **32**, 1428–1454.
16 Y. Han, M. Sun, X. Lu, K. Xu, M. Yu, H. Yang and J. Yin, *Composites, Part B*, 2024, **273**, 111241.
17 I. Kusen, A. Lee, E. A. Cuttaz, Z. K. Bailey, J. Killilea, S. M. N. Aslie, J. A. Goding and R. A. Green, *J. Mater. Chem. B*, 2024, **12**, 8929–8940.
18 M. Shur, F. Fallegger, E. Pirondini, A. Roux, A. Bichat, Q. Barraud, G. Courtine and S. P. Lacour, *ACS Appl. Bio Mater.*, 2020, **3**, 4388–4397.
19 M. Yan, L. Wang, Y. Wu, X. Liao, C. Zhong, L. Wang and Y. Lu, *ACS Appl. Mater. Interfaces*, 2023, **15**, 41310–41323.
20 T. Yang, M. Yang, C. Xu, K. Yang, Y. Su, Y. Ye, L. Dou, Q. Yang, W. Ke, B. Wang and Z. Luo, *J. Mater. Chem. B*, 2023, **11**, 3226–3235.
21 W. Wang, J. Liu, H. Li, Y. Zhao, R. Wan, Q. Wang, J. Xu and B. Lu, *Adv. Sci.*, 2025, **12**, 2414834.
22 R. Luo, K. Zhang, H. Li, Y. Cui, J. Hu, X. Zhou, W. Wang and L. Li, *Appl. Mater. Today*, 2025, **45**, 102798.
23 E. Zheng, P. Jain, H. Dong, Z. Niu, S. Chen, S. Zhong and Q. Yu, *ACS Appl. Polym. Mater.*, 2019, **1**, 3103–3114.
24 J. Y. Sun, X. Zhao, W. R. K. Illeperuma, O. Chaudhuri, K. H. Oh, D. J. Mooney, J. J. Vlassak and Z. Suo, *Nature*, 2012, **489**, 133–136.
25 S. Huang, R. Xiao, S. Lin, Z. Wu, C. Lin, G. Jang, E. Hong, S. Gupta, F. Lu, B. Chen, X. Liu, A. Sahasrabudhe, Z. Zhang, Z. He, A. J. Crosby, K. Sumaria, T. Liu, Q. Wang and S. Rao, *Nat. Commun.*, 2025, **16**, 1127.
26 H. Kandárová and P. Pôbiš, *Front. Toxicol.*, 2024, **5**, 1337468.
27 L. Schöbel, U. Özdemir and A. R. Boccaccini, *Mater. Today Chem.*, 2025, **49**, 103030.
28 L. Schöbel, M. G. Ayerbe, C. Polley, G. Arruebarrena, H. Seitz and A. R. Boccaccini, *ACS Biomater. Sci. Eng.*, 2025, **11**, 4057–4061.
29 A. Serafin, M. Culebras and M. N. Collins, *Int. J. Biol. Macromol.*, 2023, **233**, 123438.
30 K. Cysewska, J. Karczewski and P. Jasiński, *Electrochim. Acta*, 2015, **176**, 156–161.
31 M. Ghanbari, M. Salavati-Niasari and F. Mohandes, *RSC Adv.*, 2021, **11**, 18423–18431.
32 J. Skopinska-Wisniewska, M. Tuszynska, Ł. Kaźmierski, M. Bartniak and A. Bajek, *Polymers*, 2024, **16**, 2560.
33 E. W. Elsayed, A. A. El-Ashmawy, G. T. El-Bassyouni, S. M. Mousa, M. El-Manawaty and L. H. Emara, *Int. J. Biol. Macromol.*, 2023, **237**, 124147.
34 C. Tounakti, P. Decorse, F. Kouki and P. Lang, *J. Polym. Sci.*, 2023, **61**, 582–603.
35 F. Furlani, M. Montanari, N. Sangiorgi, E. Saracino, E. Campodoni, A. Sanson, V. Benfenati, A. Tampieri, S. Panseri and M. Sandri, *Biomater. Sci.*, 2022, **10**, 2040–2053.
36 D. Testore, A. Zoso, G. Kortaberria, M. Sangermano and V. Chiono, *Front. Bioeng. Biotechnol.*, 2022, **10**, 897575.
37 T. Benhalima, H. Ferfera-Harrar, A. Tahar, S. Bouchouia and K. A. Ayad, *Int. J. Biol. Macromol.*, 2025, **292**, 139300.
38 A. Manzari-Tavakoli, R. Tarasi, R. Sedghi, A. Moghimi and H. Niknejad, *Sci. Rep.*, 2020, **10**, 1–10.
39 C. Czichy, J. Spangenberg, S. Günther, M. Gelinsky and S. Odenbach, *J. Magn. Magn. Mater.*, 2020, **501**, 166395.
40 N. Abroug, L. Schöbel, A. R. Boccaccini and H. Seitz, *Gels*, 2024, **10**, 676.
41 Y. Zhang, S. Li, Z. Gao, D. Bi, N. Qu, S. Huang, X. Zhao and R. Li, *Carbohydr. Polym.*, 2023, **315**, 120953.
42 N. M. Badawi, M. Bhatia, S. Ramesh, K. Ramesh, M. Kuniyil, M. R. Shaik, M. Khan, B. Shaik and S. F. Adil, *Polymers*, 2023, **15**, 571.
43 A. Serafin, C. Murphy, M. C. Rubio and M. N. Collins, *Mater. Sci. Eng., C*, 2021, **122**, 111927.
44 M. Yao, J.-C. Hsieh, K. W. K. Tang and H. Wang, *Med-X*, 2024, **2**, 23.
45 K. Cysewska, *ChemElectroChem*, 2025, **12**, e202400459.

46 B. D. Paulsen, K. Tybrandt, E. Stavrinidou and J. Rivnay, *Nat. Mater.*, 2020, **19**, 13–26.

47 H. Ding, Y. Gu, Y. Ren, C. Hu, Q. Qiu, D. Wu, J. Mou, Z. Wu and H. Zhou, *J. Mater. Chem. C*, 2024, **12**, 3030–3052.

48 Y. Li, X. Liu, L. Han, Z. Lu and L. Liu, *J. Electroanal. Chem.*, 2023, **950**, 117904.

49 T. N. Tra, K. Fidanovski and D. Mawad, *Macromol. Mater. Eng.*, 2025, **310**, 2500019.

50 S. T. Keene, V. Gueskine, M. Berggren, G. G. Malliaras, K. Tybrandt and I. Zozoulenko, *Phys. Chem. Chem. Phys.*, 2022, **24**, 19144–19163.

51 M. T. Tourchi Moghadam and K. Cysewska, *Adv. Mater. Interfaces*, 2025, **12**, e00263.

52 A. R. Hillman, S. J. Daisley and S. Bruckenstein, *Electrochem. Commun.*, 2007, **9**, 1316–1322.

53 M. Bianchi, A. De Salvo, M. Asplund, S. Carli, M. Di Lauro, A. Schulze-Bonhage, T. Stieglitz, L. Fadiga and F. Biscarini, *Adv. Sci.*, 2022, **9**, 2104701.

54 X. Cui, J. F. Hetke, J. A. Wiler, D. J. Anderson and D. C. Martin, *Sens. Actuators, A*, 2001, **93**, 8–18.

55 B. Sarker, R. Singh, T. Zehnder, T. Forgber, C. Alexiou, I. Cicha, R. Detsch and A. R. Boccaccini, *J. Bioact. Compat. Polym.*, 2017, **32**, 309–324.

56 Z. Ferjaoui, R. López-Muñoz, S. Akbari, F. Chandad, D. Mantovani, M. Rouabhia and R. D. Fanganiello, *Biomedicines*, 2024, **12**, 1510.

57 S. Liu, H. Yang, D. Chen, Y. Xie, C. X. Tai, L. Wang, P. Wang and B. Wang, *Regen. Biomater.*, 2022, **9**, rbac038.

58 L. Benny Mattam, A. Bijoy, D. Abraham Thadathil, L. George and A. Varghese, *ChemistrySelect*, 2022, **7**, e202201765.

59 J. Yu, F. Tian, W. Wang, R. Wan, J. Cao, C. Chen, D. Zhao, J. Liu, J. Zhong, F. Wang, Q. Liu, J. Xu and B. Lu, *Chem. Mater.*, 2023, **35**, 5936–5944.

60 F. Wang, Y. Xue, X. Chen, P. Zhang, L. Shan, Q. Duan, J. Xing, Y. Lan, B. Lu, J. Liu, F. Wang, Y. Xue, X. Chen, P. Zhang, L. Shan, Q. Duan, J. Xing, J. Liu, B. Lu, J. Key and Y. Lan, *Adv. Funct. Mater.*, 2023, 2314471.

61 Y. Liu, J. Liu, S. Chen, T. Lei, Y. Kim, S. Niu, H. Wang, X. Wang, A. M. Foudeh, J. B. H. Tok and Z. Bao, *Nat. Biomed. Eng.*, 2019, **3**, 58–68.

62 B. Lu, H. Yuk, S. Lin, N. Jian, K. Qu, J. Xu and X. Zhao, *Nat. Commun.*, 2019, **10**, 1–10.

63 Y. Han, M. Sun, X. Lu, K. Xu, M. Yu, H. Yang and J. Yin, *Composites, Part B*, 2024, **273**, 111241.

64 J. Herron, A. Kullmann, T. Denison, W. K. Goodman, A. Gunduz, W. J. Neumann, N. R. Provenza, M. M. Shanechi, S. A. Sheth, P. A. Starr and A. S. Widge, *Nat. Biomed. Eng.*, 2024, **9**, 606–617.

65 C. Wu, M. Alizadeh, M. K. Kramer, M. B. Kroen, R. Ziechmann, F. B. Mohamed, Q. Wu and C. L. Johnson, *Oper. Neurosurg.*, 2025, **29**, 517–525.